

The nature and energetics of AGN-driven perturbations in the hot gas in the Perseus Cluster

I. Zhuravleva,^{1,2★} E. Churazov,^{3,4} P. Arévalo,⁵ A. A. Schekochihin,^{6,7} W. R. Forman,⁸
S. W. Allen,^{1,2,9} A. Simionescu,¹⁰ R. Sunyaev,^{3,4} A. Vikhlinin⁸ and N. Werner^{1,2}

¹Kavli Institute for Particle Astrophysics and Cosmology, Stanford University, 452 Lomita Mall, Stanford, CA 94305-4085, USA

²Department of Physics, Stanford University, 382 Via Pueblo Mall, Stanford, CA 94305-4060, USA

³Max Planck Institute for Astrophysics, Karl-Schwarzschild-Strasse 1, D-85741 Garching, Germany

⁴Space Research Institute (IKI), Profsoyuznaya 84/32, Moscow 117997, Russia

⁵Instituto de Física y Astronomía, Facultad de Ciencias, Universidad de Valparaíso, Gran Bretaña N 1111, Playa Ancha, Valparaíso, Chile

⁶Rudolf Peierls Centre for Theoretical Physics, University of Oxford, 1 Keble Rd, Oxford OX1 3NP, UK

⁷Merton College, University of Oxford, Merton St, Oxford OX1 4JD, UK

⁸Harvard-Smithsonian Center for Astrophysics, 60 Garden Street, Cambridge, MA 02138, USA

⁹SLAC National Accelerator Laboratory, 2575 Sand Hill Road, Menlo Park, CA 94025, USA

¹⁰Japan Aerospace Exploration Agency, 3-1-1 Yoshinodai, Sagami-hara, Kanagawa 252-5210, Japan

Accepted 2016 February 29. Received 2016 February 29; in original form 2016 January 6

ABSTRACT

Cores of relaxed galaxy clusters are often disturbed by AGN. Their *Chandra* observations revealed a wealth of structures induced by shocks, subsonic gas motions, bubbles of relativistic plasma, etc. In this paper, we determine the nature and energy content of gas fluctuations in the Perseus core by probing statistical properties of emissivity fluctuations imprinted in the soft- and hard-band X-ray images. About 80 per cent of the total variance of perturbations on ~ 8 –70 kpc scales in the core have an isobaric nature, i.e. are consistent with subsonic displacements of the gas in pressure equilibrium with the ambient medium. The observed variance translates to the ratio of energy in perturbations to thermal energy of ~ 13 per cent. In the region dominated by weak ‘ripples’, about half of the total variance is associated with isobaric perturbations on scales of a few tens of kpc. If these isobaric perturbations are induced by buoyantly rising bubbles, then these results suggest that most of the AGN-injected energy should first go into bubbles rather than into shocks. Using simulations of a shock propagating through the Perseus atmosphere, we found that models reproducing the observed features of a central shock have more than 50 per cent of the AGN-injected energy associated with the bubble enthalpy and only about 20 per cent is carried away with the shock. Such energy partition is consistent with the AGN-feedback model, mediated by bubbles of relativistic plasma, and supports the importance of turbulence in the cooling–heating balance.

Key words: methods: observational – methods: statistical – techniques: image processing – galaxies: clusters: intracluster medium – X-rays: galaxies: clusters.

1 INTRODUCTION

Cores of clusters of galaxies are often perturbed by powerful jets from central supermassive black holes. Interacting with intracluster gas, these jets inflate bubbles of relativistic plasma, which expel the hot gas, producing cavities in the X-ray images of clusters (e.g. Boehringer et al. 1993; Churazov et al. 2000; McNamara et al. 2000; McNamara & Nulsen 2007; Bîrzan et al. 2012; Fabian 2012; Hlavacek-Larrondo et al. 2012). The initial rapid expansion

of the bubbles may drive shocks that propagate through intracluster medium (ICM) and heat the gas (e.g. Fabian et al. 2003; Forman et al. 2007; Randall et al. 2015; Reynolds, Balbus & Schekochihin 2015). With time, rapid expansion decelerates and the bubbles continue to grow subsonically until they start rising buoyantly in the cluster atmosphere, uplifting cool gas, exciting gravity waves, and driving turbulence (Churazov et al. 2002; Omma et al. 2004; Zhuravleva et al. 2014a). One of the alternative scenarios is that the bubbles themselves are composed of hot thermal plasma and efficiently mix with the ICM, heating the gas (e.g. Hillel & Soker 2014; Soker, Hillel & Sternberg 2015). However, magnetic fields present in the ICM are likely to stabilize the bubbles and prevent their

* E-mail: zhur@stanford.edu

mixing with the surrounding thermal gas (e.g. Ruszkowski et al. 2007). A combination of turbulent heating and turbulent mixing has also been considered (Kim & Narayan 2003; Dennis & Chandran 2005; Sharma et al. 2009) as well as heating of the gas by cosmic rays through the excitation of Alfvén waves (Pfrommer 2013).

The X-ray-brightest nearby galaxy cluster, the Perseus Cluster, provides a textbook example of radio-mode AGN feedback. Deep *Chandra* observations of the cluster unveiled distinct perturbations in the hot gas in the innermost ~ 100 kpc region, where the physical properties of the gas are governed by the powerful central AGN (Fabian et al. 2011). Namely, we clearly see bubbles of relativistic plasma, shocks, cold filaments and fluctuations induced by motions of the gas. The most recent summary of the observed features in the Perseus core can be found in Fabian et al. (2011). The statistical analysis of the fluctuations was presented in Zhuravleva et al. (2015). In this paper, we attempt to understand how the outflow energy from the central AGN is partitioned between different observed phenomena.

Here, we will describe perturbations in the hot gas through their ‘effective’ equation of state (EoS), which measures correlations between observed fluctuations of density $\delta n/n$ and temperature $\delta T/T$, expressed as

$$\frac{\delta T}{T} = (\zeta_i - 1) \left(\frac{\delta n}{n} \right), \quad (1)$$

where ζ_i is the effective adiabatic index. This correlation characterizes fluctuations of T and n relative to their mean values at a given distance from the cluster centre. It may not reflect the true EoS of the ICM. Following the simplest approach, we will consider only three types of perturbations. If conduction is suppressed, then slowly displaced gas (e.g. via gravity waves, subsonic turbulence) retains its initial entropy and stays in pressure equilibrium with the ambient gas. Therefore, with respect to this ambient gas, such perturbations will appear isobaric ($\zeta_{\text{isob.}} = 0$). Any local changes in gas entropy will also appear as isobaric perturbations. Weak shocks (sound waves) with Mach number $M - 1 \ll 1$ do not change gas entropy and, therefore, result in perturbations that appear adiabatic with $\zeta_{\text{adiab.}} = 5/3$. There are also cavities in the diffuse gas associated with bubbles of relativistic plasma, which, observationally, can be interpreted as variations of the thermal gas density at constant temperature, i.e. isothermal fluctuations with $\zeta_{\text{isoth.}} = 1$.

The X-ray emissivity per unit volume is

$$f(x, y, z) = n^2 \Lambda(T), \quad (2)$$

where $\Lambda(T)$ is the X-ray emissivity in a given energy band. In the soft band (e.g. 0.5–4 keV for a gas with temperature 2–10 keV), X-ray emissivity $\Lambda(T)$ does not vary much with the gas temperature. In contrast, in a hard band (e.g. 4–8 keV), the emissivity is temperature-dependent (e.g. Forman et al. 2007; Zhuravleva et al. 2015). Therefore, each type of perturbation mentioned above will appear differently in the soft- and hard-band X-ray images. Adiabatic perturbations will have a larger amplitude in the hard band than in the soft band, while the amplitude of isobaric fluctuations will be large in the soft band and small, or even zero, in the hard band, depending on the choice of energy bands and the temperature of the cluster gas. Bubbles produce similar depressions in the X-ray images in both bands.

In this paper, we apply a statistical approach to compare the amplitude of emissivity fluctuations in two different energy bands in the Perseus Cluster by measuring the power spectra of fluctuations in both bands and their cross-spectrum. We aim to establish the nature of the observed perturbations in the cluster core, which are induced

by the central AGN, and to constrain the energy content associated with each type of perturbation. This work is accompanied by a recent analysis of fluctuations in the Virgo/M87 Cluster (Arévalo et al. 2016) and is the third paper in a series devoted to the statistical analysis of fluctuations in Perseus (see Zhuravleva et al. 2014a, 2015).

2 ISOBARIC, ADIABATIC AND ISOTHERMAL FLUCTUATIONS

We denote by $\delta f/f$ the emissivity fluctuation field in 3D, relative to the spatially smooth model. Let us assume that $\delta f/f$ can be decomposed into isobaric, adiabatic and isothermal components,

$$\frac{\delta f}{f} = \sum_i \left(\frac{\delta f}{f} \right)_i, \quad (3)$$

where i corresponds to one of the three considered types of perturbations. Of course, this trichotomy does not cover all possibilities. For instance, gas metallicity variations are not captured by it. However, equation (3) accounts for several major types of perturbations, which are expected to be present in the ICM (see Discussion). If the typical amplitude of fluctuations is small, one can link the emissivity fluctuations to the corresponding density fluctuations. Namely, for the i th type of perturbations

$$\left(\frac{\delta f}{f} \right)_i = \left(\frac{\delta n}{n} \right)_i \left[2 + (\zeta_i - 1) \frac{d \ln \Lambda(T)}{d \ln T} \right] \equiv \left(\frac{\delta n}{n} \right)_i w_i, \quad (4)$$

where $\zeta_i = 0, 5/3$ or 1 for isobaric, adiabatic and isothermal fluctuations, respectively, and

$$w_i = \left[2 + (\zeta_i - 1) \frac{d \ln \Lambda(T)}{d \ln T} \right]. \quad (5)$$

For a given type of perturbations, the ratio of emissivity fluctuation fields measured in two different energy bands a and b is independent of density perturbations $(\delta n/n)_i$, namely,

$$\frac{(\delta f_b/f_b)_i}{(\delta f_a/f_a)_i} = \frac{w_{b,i}}{w_{a,i}} = \frac{2 + (\zeta_i - 1) \frac{d \ln \Lambda_b(T)}{d \ln T}}{2 + (\zeta_i - 1) \frac{d \ln \Lambda_a(T)}{d \ln T}}. \quad (6)$$

Fig. 1 shows the ratio of emissivities in the soft (0.5–4 keV) and hard (4–8 keV) bands (the choice of the bands is justified in Appendix A), assuming the abundance of heavy elements $Z = 0.5 Z_\odot$ (relative to the solar abundance of heavy elements from Anders & Grevesse 1989), redshift $z = 0.01755$ and galactic H I column density $1.35 \times 10^{21} \text{ cm}^{-2}$ (Dickey & Lockman 1990; Kalberla et al. 2005), which correspond to those of the Perseus Cluster. In a gas with the range of temperatures 3–6.5 keV, characteristic for the Perseus core, $(\delta f_b/f_b)_i/(\delta f_a/f_a)_i \approx 1.3, 1$ and ≈ 0.5 for pure adiabatic, isothermal and isobaric perturbations, respectively. Substantial difference between the curves allows one to distinguish between different types of perturbations using observations, which is more difficult to do for hotter objects. Note that the gas metallicity in the core of Perseus varies between ~ 0.7 and ~ 0.3 (Fabian et al. 2011; Werner et al. 2013). However, we have verified that these variations do not affect the ratios in Fig. 1 if the gas temperature is larger than ~ 2 –3 keV.

In practice, we are dealing not with the 3D emissivity fluctuation field, but with the projection of this field on to the plane of the sky. However, for a nearly isothermal cluster, the ratio of surface brightness fluctuations in two energy bands is expected to follow equation (6), provided that a single type of perturbation is dominating a region of interest (e.g. Churazov et al., in preparation).

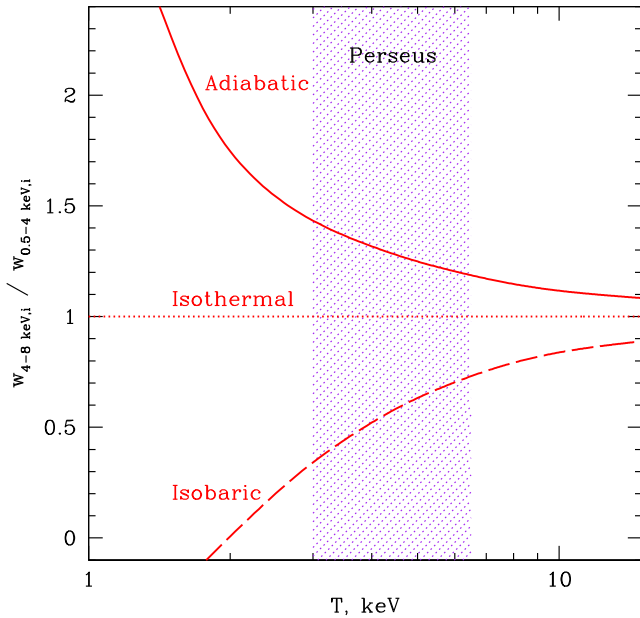


Figure 1. The ratio (equation 6) of emissivity perturbations in two energy bands, 0.5–4 keV and 4–8 keV, as a function of gas temperature, assuming that the perturbations are pure isobaric, isothermal or adiabatic. The purple dotted region shows the range of gas temperatures in the Perseus Cluster. Redshift, galactic H I column density and the abundance of heavy elements $Z = 0.5 Z_{\odot}$ (relative to the solar abundance of heavy elements; see Anders & Grevesse (1989)) of Perseus are used.

The residual images (the initial images divided by the best-fitting spherically symmetric β -models of the surface brightness) of the Perseus Cluster in 0.5–4 keV and 4–8 keV bands, Fig. 2 (see Section 3 for details), show that the amplitude of the spiral-like feature is larger in the soft band than in the hard band, hinting at an isobaric nature of this feature (see Fig. 1). However, in some regions around the central bubbles, the amplitude of perturbations is larger in the hard band, suggesting they have an adiabatic nature. Such visual examination allows us to guess the nature of large-scale and large-amplitude fluctuations. For the less prominent fluctuations that we cannot easily identify in the images, a different, statistical approach is needed.

Assuming that $\delta f/f$ is a homogeneous and isotropic random field, we calculate the cross-spectrum (real part) $P_{k,ab}$ of emissivity fluctuations in two energy bands a and b as

$$P_{k,ab} = \text{Re} \left[\left(\frac{\delta \hat{f}_a}{f_a} \right) \cdot \left(\frac{\delta \hat{f}_b}{f_b} \right)^* \right], \quad (7)$$

where k is a wavenumber and $|\delta \hat{f}/f|$ is the Fourier transform of $\delta f/f$ in both bands. In practice, in order to avoid the adverse effects of non-periodic data and gaps in the exposure map, the calculations are done in real space using a modified Δ variance method to measure the surface brightness fluctuations in images in both bands (Ossenkopf, Krips & Stutzki 2008; Arévalo et al. 2012). First, fluctuations at a given spatial scale $1/k$ are singled out and then the variance of the convolved image is calculated, namely,

$$P_{k,ab} = \left\langle \left(\frac{\delta f_a}{f_a} \right)_{1/k} \left(\frac{\delta f_b}{f_b} \right)_{1/k} \right\rangle \quad (8)$$

where $\langle \rangle$ denotes averaging over space, and $(\delta f_a/f_a)_{1/k}$ is the emissivity fluctuation field in the energy band a , filtered to keep only spatial scales $\sim 1/k$. Equation (8) essentially provides an estimate

of the conventional cross-power spectrum (equation 7) convolved with a smoothing kernel (see e.g. Arévalo et al. 2012; Zhuravleva et al. 2012; Zhuravleva et al. 2014b, for details). Measuring power spectra $P_{k,aa}$ and $P_{k,bb}$ in both bands and the cross-spectrum $P_{k,ab}$, a scale-dependent correlation coefficient (coherence),

$$C(k) = \frac{P_{k,ab}}{\sqrt{P_{k,aa} P_{k,bb}}}, \quad (9)$$

and a relative amplitude (ratio) of fluctuations in two energy bands,¹

$$R(k) = \frac{P_{k,ab}}{P_{k,aa}} = C \sqrt{\frac{P_{k,bb}}{P_{k,aa}}}, \quad (10)$$

can be calculated.

Of course, in the real ICM, instead of pure isobaric, adiabatic or isothermal perturbations, we have a mixture of different types of perturbations.² Using equations (3) and (4), it is easy to rewrite expected values of C and R for any given mix of these three types of perturbations via the power spectra $S_{k,i}$ of the density fluctuation fields $(\delta n/n)_i$, assuming that these fields are uncorrelated. Calculating C and R in terms of this decomposition, we find

$$C(k) = \frac{\sum_i S_{k,i} w_{a,i} w_{b,i}}{\sqrt{\sum_i S_{k,i} w_{a,i}^2} \sqrt{\sum_i S_{k,i} w_{b,i}^2}} = \frac{\sum_i \alpha_i^2 w_{a,i} w_{b,i}}{\sqrt{\sum_i \alpha_i^2 w_{a,i}^2} \sqrt{\sum_i \alpha_i^2 w_{b,i}^2}}, \quad (11)$$

and

$$R(k) = \frac{\sum_i S_{k,i} w_{a,i} w_{b,i}}{\sum_i S_{k,i} w_{a,i}^2} = \frac{\sum_i \alpha_i^2 w_{a,i} w_{b,i}}{\sum_i \alpha_i^2 w_{a,i}^2}, \quad (12)$$

where $\alpha_i^2 = S_{k,i} / \sum_j S_{k,j}$ are normalized spectra. Clearly, if one type of fluctuation dominates, then $C = 1$ and R coincides with the values given in equation (6) and shown in Fig. 1. Otherwise, $|C| < 1$ and R has a value intermediate between these curves.

Since $\alpha_{\text{isob.}}^2 + \alpha_{\text{adiab.}}^2 + \alpha_{\text{isoth.}}^2 = 1$, the maps of the expected values C and R can be calculated as functions of two parameters $\alpha_{\text{isob.}}$ and $\alpha_{\text{adiab.}}$, setting $\alpha_{\text{isoth.}} = \sqrt{1 - \alpha_{\text{isob.}}^2 - \alpha_{\text{adiab.}}^2}$ for any combination of the three types of perturbations. Then, measuring C and R through the observed power and cross-spectra of emissivity fluctuations, equations (9) and (10), and finding these values on C and R maps, the relative contribution of each type of perturbations to the observed total variance of the fluctuations at a given wavenumber k can be obtained.

If the amplitude of fluctuations is large, \sim few tens per cent, C and R in adiabatic and isobaric cases may differ from those shown in Fig. 1. Our simulations (see Appendix B) show that as long as the amplitude of density fluctuations is $\lesssim 15$ per cent in gas with temperature > 3 keV, the ratio is consistent with the values in the limit of small-amplitude perturbations.

3 DATA PROCESSING, IMAGES AND POWER SPECTRA

We use public *Chandra* data of the Perseus Cluster with total cleaned exposure ≈ 1.4 Ms. We assume the redshift of the Perseus Cluster

¹ As the number of photons in the soft band is often larger than in the hard band, the power spectrum of fluctuations in the soft band $P_{k,aa}$ is used in the denominator in equation (10).

² Possibly a continuum of values of ζ_i in equation (6).

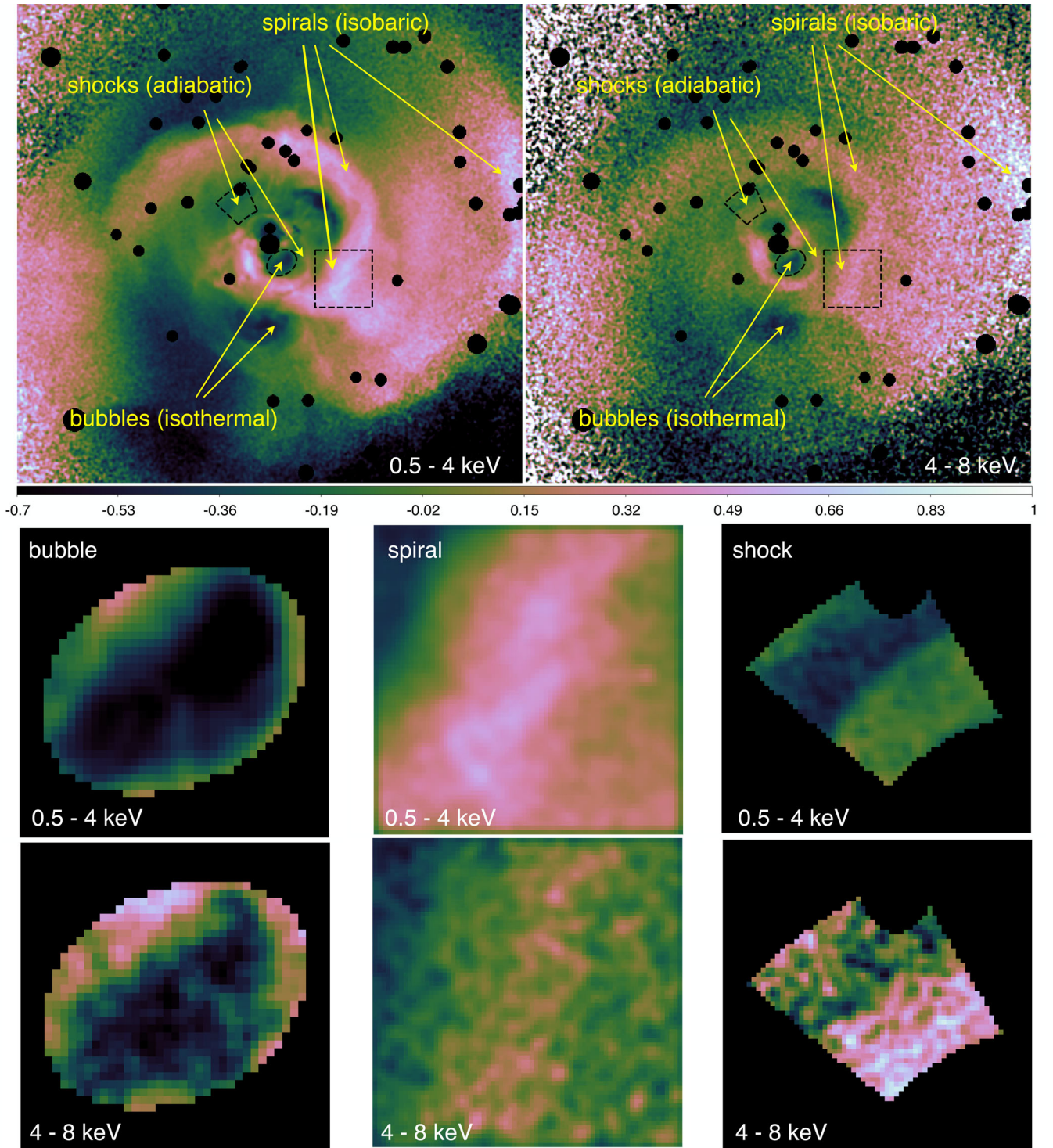


Figure 2. *Chandra* images of the core ($\approx 200 \times 200$ kpc, or 9.6×9.6 arcmin) of the Perseus Cluster divided by the spherically symmetric β -model in the 0.5–4 keV (top left) and 4–8 keV (top right) bands. Point sources and the central AGN are excised. Arrows point to the prominent features identified in previous studies. Dashed regions indicate selected regions with a shock, a bubble and a spiral. They are enlarged in the middle and bottom panels. The colour scales of the image pairs are the same. For display purposes, all images are lightly smoothed with a 2 arcsec Gaussian.

$z = 0.01755$ and the angular diameter distance 71.5 Mpc. 1 arcmin corresponds to a physical scale 20.81 kpc. The total Galactic H I column density is $1.35 \times 10^{21} \text{ cm}^{-2}$ (Dickey & Lockman 1990; Kalberla et al. 2005). The initial data reduction, the details of image processing and the treatment of point sources are described

in detail in Zhuravleva et al. (2015, Section 2). Both images, in the 0.5–4 keV and 4–8 keV bands, are treated identically. Masking out point sources and the central AGN, the best-fitting spherically symmetric β -models of surface brightness are obtained. Their parameters are $r_c = 1.28$ (1.48) arcmin and $\beta = 0.53$ (0.49) in the

soft (hard) band. The images of Perseus divided by the corresponding underlying β -models in both bands are shown in Fig. 2. There are many structures produced by gas perturbations of different nature. The large-scale structures whose nature was identified through ‘X-arithmetic’ analysis (Churazov et al., in preparation) are marked with arrows.

The power and cross-spectra of surface brightness fluctuations in the X-ray images are measured using the modified Δ variance method (Ossenkopf et al. 2008; Arévalo et al. 2012). Subtracting Poisson noise and correcting for the suppression factor associated with $2D \rightarrow 3D$ deprojection, which depends only on the global geometry of the cluster, the 3D power spectra of the volume emissivity fluctuations in both bands, $P_{k,aa}$ and $P_{k,bb}$, and the cross-spectrum $P_{k,ab}$ are calculated. Instead of power spectra, we will show the characteristic amplitude defined as $A_{k,ab} = \sqrt{4\pi P_{k,ab} k^3}$ (similarly for $A_{k,aa}$ and $A_{k,bb}$) that is a proxy for the rms of emissivity fluctuations $\delta f/f$ at a given wavenumber $k = 1/l$. For the data set considered below, the values of $P_{k,ab}$ are always positive.

Similar analysis was already applied to the analysis of density fluctuations in the AWM7 Cluster (Sanders & Fabian 2012), the Coma Cluster (Churazov et al. 2012), the Perseus Cluster (Zhuravleva et al. 2015), the Virgo Cluster (Arévalo et al. 2016) and the Centaurus Cluster (Walker, Sanders & Fabian 2015). Slightly different approaches have been used to measure pressure fluctuations in the Coma Cluster (Schuecker et al. 2004) and temperature fluctuations in a sample of clusters (Gu et al. 2009). The only difference here from our previous analyses is that here the $2D \rightarrow 3D$ deprojection is calculated at each pixel instead of averaged over an area of interest. The underlying β -models are slightly different in two bands since the gas temperature changes with radius. Therefore, we calculate the geometrical correction (the suppression factor) individually for each band. Uncertainties associated with the choice of the underlying β -model and inhomogeneous exposure coverage (see details in Zhuravleva et al. 2015, Section 6) are estimated and taken into account for each fluctuation spectrum presented here.

The analysis of X-ray surface brightness fluctuations directly measures fluctuations of the volume emissivity convolved with *Chandra* response. In the soft band a , where the temperature dependence of X-ray emissivity is weak, $P_{k,aa} \approx 4S_{k,aa}$, provided that $\delta n/n \ll 1$ (Churazov et al. 2012). In the hard band, the temperature dependence is significant, and, therefore, the spectrum of the emissivity fluctuations does not correspond to the spectrum of pure density fluctuations.

4 RESULTS

Here we first test our analysis technique in selected regions of the Perseus Cluster that are dominated by prominent, previously identified structures, such as a shock, a bubble or a spiral (Section 4.1). Next, we apply the same analysis to fluctuations in the central (7×7 arcmin) region, strongly perturbed by AGN activity, as well as in the region dominated by ripple-like structures (Section 4.2). For each of these cases, we investigate the effects of systematic uncertainties, such as inhomogeneous exposure coverage and the choice of the underlying model (for details, see section 6 of Zhuravleva et al. 2015). We use a uniform weighting scheme when calculating rms of fluctuations present in filtered images, and a spherically symmetric β -model as the underlying model. Our experiments show that various systematic uncertainties do not change our conclusions, although some specific numbers may differ for different weightings or underlying models.

We also tested the cross-spectra technique on simulated X-ray images containing shocks and sound waves (see Appendix C). These tests show that our analysis is able to recover the nature of the dominant type of fluctuation even if the amplitude of the fluctuations is small, \sim a few per cent.

4.1 Special cases: shock, bubble, spiral

Residual images of three selected regions are shown in Fig. 2. All three regions are within the innermost 30 kpc, where the number of photon counts is large and the gas temperature is ≈ 3 –3.4 keV. For a mean temperature of 3.2 keV, we calculate the C and R maps for all possible combinations of isothermal, adiabatic and isobaric perturbations (Fig. 3, bottom panels). Amplitudes of the volume emissivity fluctuations in the soft and hard bands and cross-amplitude as functions of wavenumber are shown in the top panels of Fig. 3.

In the region with a shock (spiral), the amplitude in the hard band is larger (smaller) than in the soft band over a broad range of scales. Emissivity fluctuations have comparable amplitudes in both bands in the ‘bubble’ region.

Fluctuations associated with the shock region have $C \simeq 0.90$ – 0.98 and $R \simeq 1.3$ – 1.8 on scales between 8 and 20 kpc. On these scales we are effectively comparing the density and temperature of the pre-shock gas to those in the shock-heated gas. The shell has a thickness of ~ 8 kpc. The locus of these values on the C and R maps is shown with the black ellipses. They lie within the area dominated by adiabatic perturbations.

Emissivity fluctuations in the region containing the bubble have $C \simeq 0.92$ – 0.98 and $R \simeq 0.90$ – 1.05 on scales between 4 and 10 kpc. The locus of these values (blue ellipse in Fig. 3) reveals a predominantly isothermal nature of these perturbations with small contamination of adiabatic and isobaric fluctuations, associated with the shock around the bubble and displaced gas, respectively, imprints of which remain in the selected region.

In the region with a spiral structure, we find $C \simeq 0.8$ – 0.9 and $R \simeq 0.50$ – 0.51 on 10–20 kpc scales. The locus of these values (white ellipse in Fig. 3) confirms the isobaric nature of these fluctuations.

These experiments show that even if the uncertainties are large, the cross-spectra method robustly identifies the dominant type of fluctuations in the X-ray emissivity.

4.2 Central, AGN-dominated region

We now proceed with the analysis of the central $r = 3.5$ arcmin (≈ 70 kpc) region, which appears to be disturbed by several types of perturbations and is dominated by a prominent spiral structure and bubbles (Fig. 4). Masking out point sources and the central AGN, we measure the amplitude of the volume emissivity fluctuations in both 0.5–4 keV and 4–8 keV bands, the coherence C and the ratio R shown in the top panels in Fig. 5. Black ellipse on the $C - R$ map in the bottom panel in Fig. 5 shows the locus of the measured values $C \simeq 0.80$ – 0.93 and $R \simeq 0.50$ – 0.55 on scales ~ 8 –70 kpc. The approximate centre of the locus gives $\alpha_{\text{adiab.}} \simeq 0.28$, $\alpha_{\text{isob.}} \simeq 0.88$ and the corresponding $\alpha_{\text{isoth.}} = \sqrt{1 - \alpha_{\text{adiab.}}^2 - \alpha_{\text{isob.}}^2} \simeq 0.38$. Therefore, $\alpha_{\text{isob.}}^2 \approx 80$ per cent of the total variance can be attributed to isobaric type of fluctuations, less than $\alpha_{\text{adiab.}}^2 \approx 8$ per cent of the variance to adiabatic and $\alpha_{\text{isoth.}}^2 \approx 14$ per cent to isothermal perturbations. Exclusion of the innermost bubbles and shocks from the central $r = 3.5$ arcmin region tilts the results towards even larger isobaric fraction.

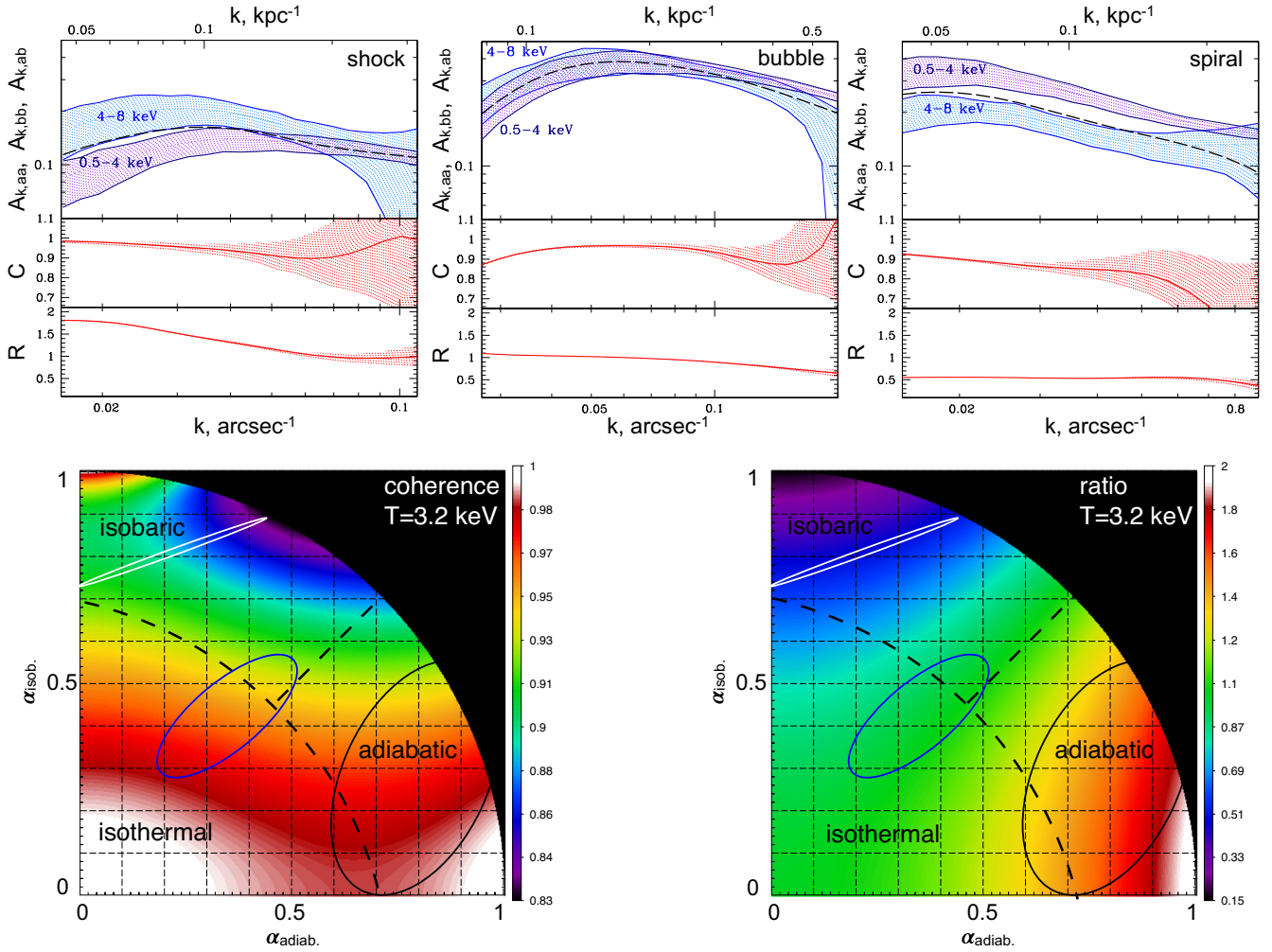


Figure 3. Results of the cross-spectra analysis in regions with the shock (top left), bubble (top middle) and spiral (top right) (see Fig. 2). Top row: amplitude of the volume emissivity fluctuations, in the soft, $A_{k,aa}$, (purple) and hard, $A_{k,bb}$, (blue) bands and the cross-amplitude, $A_{k,ab}$, (black dashed curve); coherence C and ratio R obtained from the observed spectra [equations (9) and (10)]. Blue and purple dotted regions show 1σ statistical and stochastic uncertainties. For clarity, we do not plot the uncertainties on the cross-amplitudes. Our conservative estimates of statistical uncertainties on the measured C and R are shown with the dotted red regions. Bottom row: maps of coherence C (left) and ratio R (right) for a mixture of isobaric, adiabatic and isothermal perturbations in the 3.2 keV gas. Colour bars show the values of C and R [equations (11) and (12)]. The dashed grid shows the values of α_i , associated with each type of fluctuation (see Section 2). X-axis: contribution of adiabatic fluctuations α_{adiab} ; Y-axis: contribution of isobaric fluctuations α_{isob} . The contribution of isothermal fluctuations is $\alpha_{\text{isoth}} = \sqrt{1 - \alpha_{\text{adiab}}^2 - \alpha_{\text{isob}}^2}$. The maps are schematically divided into three regions where one of the types of perturbations is dominant in terms of total variance. Ellipses show the regions of α_{isob} , α_{adiab} , and α_{isoth} , that correspond to the values of R and C taken from the figures in the top row. Black ellipse: the region with shock, blue ellipse: bubble, white ellipse: spiral. The size of each ellipse reflects the uncertainties associated with Poisson noise, the choice of the underlying model and the choice of the weighting scheme in calculating the power spectra. The locus of C and R is in the adiabatic area if measured in the region with the shock in Perseus, in the isobaric area if obtained from the region with spiral structure and in the isothermal area when the region with the bubble is considered.

The unsharp masking of the Perseus image shows approximate concentric features, so-called ripples, that are narrow in the radial direction and wide in the azimuthal direction (Fabian et al. 2006; Sanders & Fabian 2007). The width of the ripples in the radial direction is roughly 5–15 kpc (see e.g. Fig. 4). Some of the ripples are associated with the brightest and most clearly defined parts of the spiral structure and have an isobaric nature. However, the nature of those ripples that are not associated with the spiral structure is not clear. Two possible scenarios for their origin have been discussed: weak shocks and sound waves propagating through the gas (see e.g. Sanders & Fabian 2007; Graham, Fabian & Sanders 2008a; Fabian et al. 2011, and references therein) or stratified turbulence (Zhuravleva et al. 2014b, 2015). Aiming to understand the

physical origin of the ripples, we repeated the cross-spectra analysis of the emissivity fluctuations in the region from which we excised the ripples associated with prominent spiral, bubbles, shocks and filaments (see the dotted region in Fig. 4). The results, shown in Fig. 5 (white ellipse), reveal that the mean value of $\alpha_{\text{adiab}} \approx 0.23$, $\alpha_{\text{isob}} \approx 0.7$ and $\alpha_{\text{isoth}} \approx 0.67$. Therefore, $\alpha_{\text{isob}}^2 \approx 50$ per cent of the total variance is associated with isobaric, $\alpha_{\text{adiab}}^2 \approx 5$ per cent with adiabatic and $\alpha_{\text{isoth}}^2 \approx 45$ per cent with isothermal perturbations on scales ~ 12 –30 kpc. In other words, the variance presumably induced by the slow motions of the gas in the cluster atmosphere and bubbles constitutes the largest fraction of the total energy in this region on scales larger than 12 kpc. This conclusion does not exclude the presence of ripples associated with shocks and sound waves.

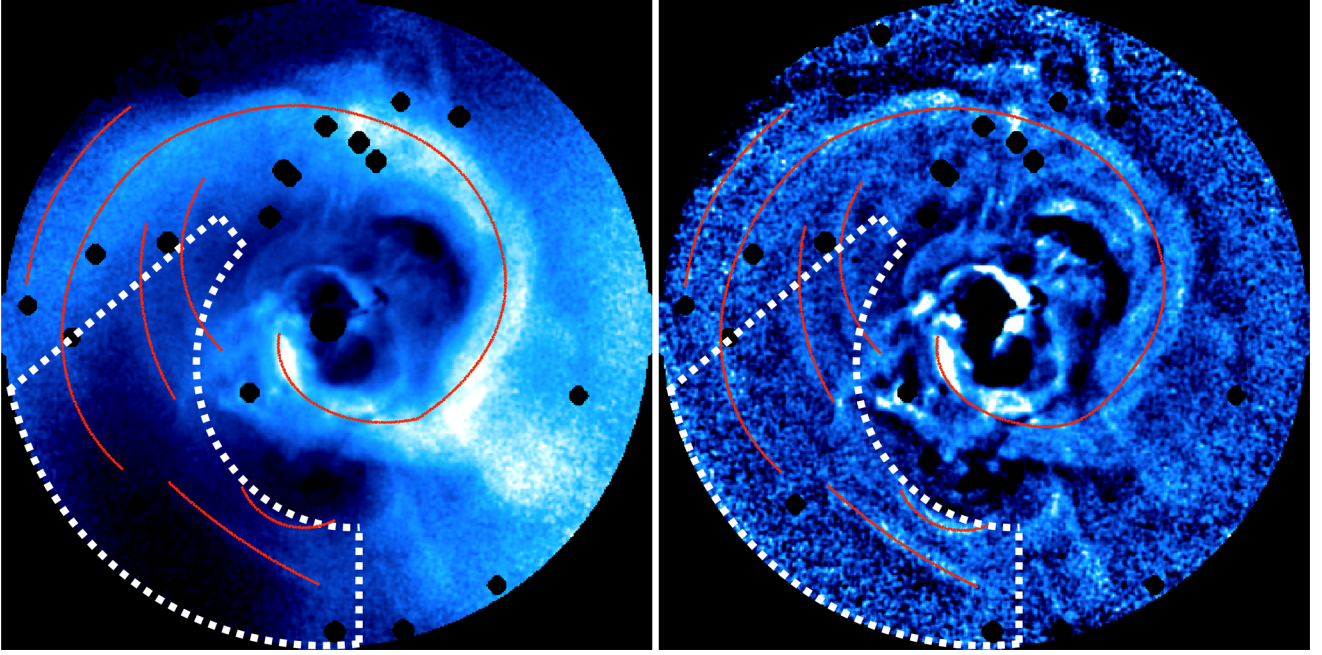


Figure 4. Image of the central $r = 3.5$ arcmin (≈ 70 kpc) region of the Perseus Cluster divided by the spherically symmetric β -model of the surface brightness (left) and additionally filtered with the high-pass filter (right); see details in section 6.1 in Zhuravleva et al. (2014a). Point sources and the central AGN are excised. The most prominent ripples are schematically highlighted with red curves. A selected region of the cluster with ripples and without obvious bubbles, central shock, filaments or prominent spiral structure, is shown with dotted boundaries. This region is used in Section 4.2 to test the properties of this subset of ripples.

However, energetically such perturbations appear to be subdominant. An interesting question would be to understand the nature of fluctuations on smaller scales, less than 12 kpc. Currently, the high level of Poisson noise in the hard band limits our ability to measure the amplitude of emissivity fluctuations on such small scales. For the same reason, it is difficult to perform the analysis for individual ripples. To address these questions, at least twice longer *Chandra* observations would be needed.

Similar analysis applied to a region outside the inner part of Perseus, the annulus at 3.5–6 arcmin, shows that isobaric fluctuations are again the dominant contributor to the total variance on scales ~ 20 –50 kpc. In this annulus, the photon statistics in the hard band are too low to constrain the nature of perturbations on smaller scales.

5 DISCUSSION

5.1 Energetics of AGN-driven perturbations and their dissipation time-scale

The measured variance of the volume emissivity fluctuations can be translated into the total energy E_{pert} associated with AGN-induced perturbations in the gas, which we write as $E_{\text{pert}} = E_b + E_{\text{sw}} + E_{\text{gw}}$, where E_b is the energy in the fluctuations due to bubbles of relativistic plasma (isothermal perturbations), E_{sw} is the energy associated with sound waves and shocks (adiabatic perturbations) and E_{gw} is the energy in fluctuations induced by gravity waves, turbulence or any other slow displacements of the gas (isobaric perturbations). All other contributions are ignored for simplicity. It is convenient to compare these energies to the thermal energy of the gas $E_{\text{th}} = PV/(\gamma - 1) = 3PV/2$, where P is its pressure and V is the volume of the region under consideration. Clearly, for each type of perturbation $E/E_{\text{th}} \sim \langle (\delta n/n)^2 \rangle \approx \frac{1}{4} \langle (\delta f/f)^2 \rangle$ if $\delta f/f$ is measured

in soft (density) band and the perturbation amplitude is small. Let us estimate the proportionality coefficient between E/E_{th} and $\delta n/n$ in each case.

The total energy of a bubble is a sum of the internal energy and work done by the expanding bubble on the cluster gas, i.e. $E_b = \gamma_b PV_b/(\gamma_b - 1)$, where $\gamma_b = 4/3$ is the adiabatic index of the hot relativistic gas inside the bubble and V_b is the volume of the bubbles (e.g. Churazov et al. 2001). The ratio $E_b/E_{\text{th}} = \gamma_b(\gamma - 1)X_b/(\gamma_b - 1)$, where X_b is the fraction of the volume occupied by the bubbles. Assuming that the bubbles are completely devoid of thermal gas, they will correspond to density fluctuations $\delta n/n = -1$, while fluctuations in the rest of the gas are small. Hence, if the bubbles occupy a small fraction of the volume, the total variance of the gas density fluctuations in any given volume becomes $\langle (\delta n/n)_b^2 \rangle = X_b$, and, therefore (see also Arévalo et al. 2016),

$$\frac{E_b}{E_{\text{th}}} = \frac{\gamma_b(\gamma - 1)}{\gamma_b - 1} \left\langle \left(\frac{\delta n}{n} \right)_b^2 \right\rangle. \quad (13)$$

The total energy in sound waves is

$$E_{\text{sw}} = \int \left(\frac{\rho v^2}{2} + \frac{c_s^2 \delta \rho^2}{2\rho} \right) dV, \quad (14)$$

where $\rho = \mu m_p n$ is the gas density, $\mu = 0.61$ is the mean particle weight, m_p is the proton mass, v is the velocity of the gas in the wave and c_s is the sound speed of the gas (Landau & Lifshitz 1959). For a propagating linear plane wave $\delta \rho/\rho = \delta n/n = v/c_s$, and, therefore, the ratio of the energy in sound waves to the thermal energy is

$$\frac{E_{\text{sw}}}{E_{\text{th}}} = \gamma(\gamma - 1) \left\langle \left(\frac{\delta n}{n} \right)_{\text{sw}}^2 \right\rangle. \quad (15)$$

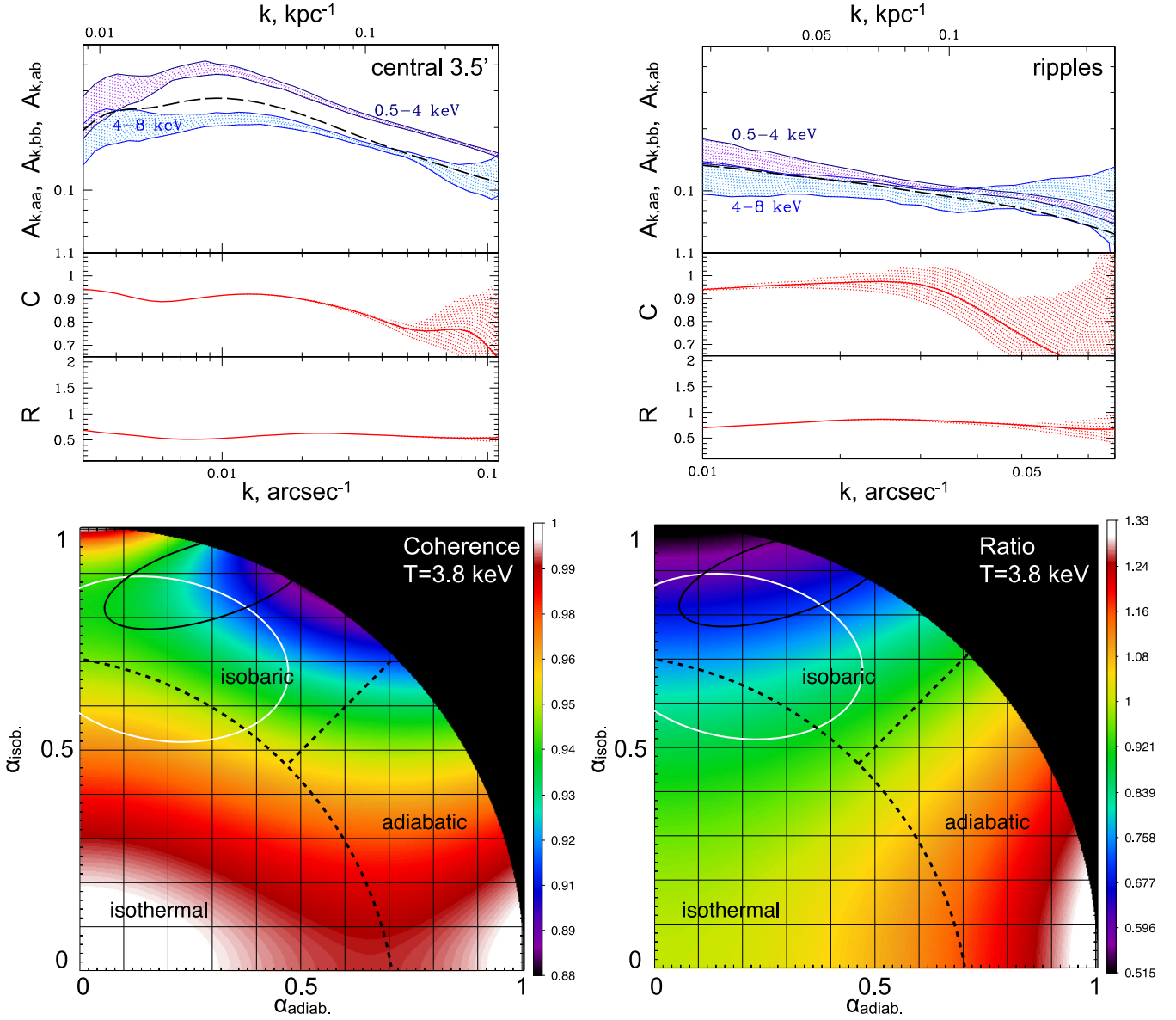


Figure 5. Results of the cross-spectra analysis in the core of the Perseus Cluster shown in Fig. 4. Left: results from the entire central $r \sim 3.5$ arcmin (~ 70 kpc) region. Right: results from the selected dotted region (Fig. 4). Top row: amplitude of the volume emissivity fluctuations in the soft and hard bands, cross-amplitudes, measured coherence C and ratio R . Bottom row: the corresponding C and R maps. Notation and colour coding are the same as in Fig. 3. The ellipses show a range of parameters that lead to the observed values of C and R . The sizes of the ellipses reflect statistical and systematic uncertainties. Black ellipse: the entire $r = 3.5$ arcmin region, white ellipse: the selected dotted region (Fig. 4). The fluctuations in the central region are predominantly isobaric.

The energy of gravity waves is

$$E_{\text{gw}} = \int \left(\frac{\rho v^2}{2} + \frac{H_p}{H_s} \frac{c_s^2 \delta \rho^2}{2\rho} \right) dV, \quad (16)$$

where H_p and H_s are pressure and entropy scale heights, respectively, the ratio of which is $H_p/H_s = 1/(\gamma - 1)$ in an isothermal cluster. In the case of propagating gravity waves, the density perturbations follow the relation $\langle (\delta n/n)_{\text{gw}}^2 \rangle \propto (\gamma - 1) \langle (v/c_s)^2 \rangle$ on scales larger than the Ozmidov scale (see e.g. Zhuravleva et al. 2014a). Therefore, accounting for equation (16), the ratio of the energy in gravity waves to the thermal energy becomes

$$\frac{E_{\text{gw}}}{E_{\text{th}}} = \gamma \left\langle \left(\frac{\delta n}{n} \right)_{\text{gw}}^2 \right\rangle. \quad (17)$$

Since the coefficient between energy ratios and the variance of density fluctuations is a factor of a few in all cases (equations 13, 15 and 17) and the measured total variance of the fluctuations attributed to isobaric type of perturbation constitutes ≈ 80 per cent of the total variance in the inner $r = 3.5$ arcmin in Perseus (Section 4.2), we will use equation (17) to convert the variance of density fluctuations to the total energy in perturbations.

We obtain the variance $\langle (\delta n/n)^2 \rangle$ by integrating the measured 3D power spectrum of the volume emissivity fluctuations $P_{k,aa}$ in the soft ('density') band

$$\left\langle \left(\frac{\delta n}{n} \right)^2 \right\rangle = \frac{1}{2} \int_{k_{\text{min}}}^{k_{\text{max}}} P_{k,aa} 4\pi k^2 dk. \quad (18)$$

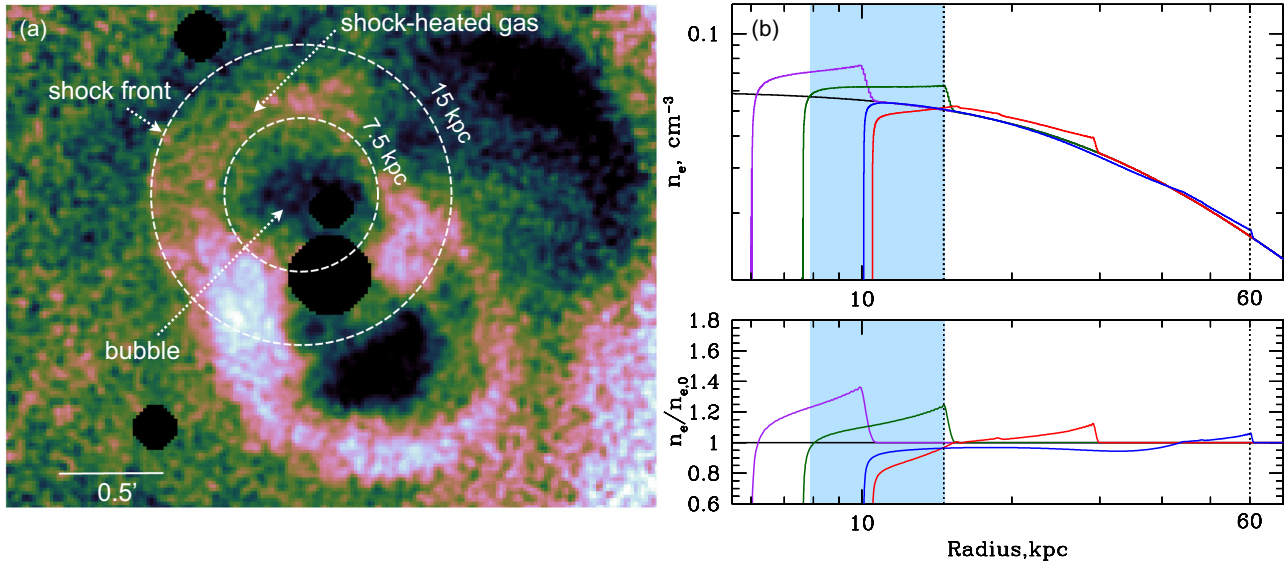


Figure 6. Features produced by the AGN outburst in the innermost region in the Perseus Cluster. (a) the image of the innermost region of the Perseus Cluster ($\sim 60 \times 60$ kpc) in the 4–8 keV band divided by the best-fitting β -model. Point sources and the central AGN are excised. Dashed circles indicate one of the inner bubbles with the size $r \approx 7.5$ kpc and a shock front around it at $r \approx 15$ kpc from the bubble centre. (b) Snapshots of simulated density profiles perturbed by a spherical shock, which propagates through the gas in the Perseus Cluster. The shock is driven by an outburst with power $3 \times 10^{44} \text{ erg s}^{-1}$. Black curve shows the initial (unperturbed) density profile, while the colour curves show the profiles at different times after the energy injection starts. The dotted vertical lines indicate the radii of 15 and 60 kpc. The former corresponds to the position of the shock around the inner bubble in Perseus, while the latter shows the approximate location of the distinct ripples. For the shock at ≈ 15 kpc, the size of the region with the shock-heated gas (shell) is indicated with the shaded blue region. The ratio of the perturbed density to the initial one is shown in the bottom panel.

$P_{k,aa}$ converted to the amplitude $A_{k,aa}$ is shown in the left panel in Fig. 5. The integration over the entire range of scales that we probe with our measurements gives $\langle (\delta n/n)^2 \rangle \sim 0.08$, which implies that the energy in perturbations is ~ 13 per cent of the thermal energy. This estimate should be considered as a lower limit.

Zhuravleva et al. (2014b) showed that there is an approximate balance between local radiative cooling rate and turbulent dissipation rate in the core of the Perseus Cluster. Therefore, one can write $E_{\text{pert}}/t_{\text{diss}} \approx E_{\text{th}}/t_{\text{cool}}$, where t_{diss} is the dissipation time-scale needed to convert the energy in perturbations into heat through turbulent dissipation in order to maintain the balance of cooling and turbulent energy dissipation and

$$t_{\text{cool}} = \frac{3(n_e + n_i)k_B T}{2n_e n_i \Lambda(T)} \quad (19)$$

is the cooling time (n_e and n_i are the number densities of electrons and ions, respectively, and k_B is the Boltzmann constant). In the inner $r = 3.5$ arcmin in Perseus, the cooling time varies between 0.45 and 3 Gyr (e.g. Zhuravleva et al. 2014b). Therefore, the dissipation time is given by $t_{\text{diss}} \sim t_{\text{cool}} E_{\text{pert}}/E_{\text{th}} \approx 0.06 - 0.4$ Gyr. This is consistent with the dissipation time-scale in the core of the Virgo Cluster, which was estimated using the same technique by Arévalo et al. (2016).

5.2 The partition of energy from the central AGN outburst

We showed above that isobaric perturbations are energetically dominant in the inner region of the Perseus Cluster, where gas properties are strongly affected by the central AGN. If these isobaric perturbations are associated with slow gas displacements induced by buoyantly rising and expanding bubbles of relativistic plasma, then the energy from the AGN outburst should be partitioned so that the largest fraction of it goes to the bubbles rather than to shocks or

the compressed, shock-heated gas around the bubbles. The partition of the energy depends on the duration of the outburst and on the total outburst energy. Forman et al. (2015) discuss two extreme scenarios: a short-duration outburst, which produces small bubbles surrounded by hot, low-density gas and strong shocks, which carry out most of the AGN energy, and a long-duration outburst, which produces weaker shocks and larger bubbles, which store most of the AGN energy surrounded by the cooler gas. Using 1D numerical simulations of a spherical shock propagating into the gas, Forman et al. (2015) showed that the observational properties of the most prominent shock in the centre of the M87/Virgo Cluster are best described with a long-outburst model with total energy outburst $\sim 5 \times 10^{57} \text{ erg}$ lasting ~ 2 Myr. In this model, ≈ 50 per cent of the injected energy goes into the thermal energy of the bubble and ≈ 20 per cent is carried away by the shock. Admittedly, the modelling is done under strong assumptions about the source geometry, initial density and temperature profiles, (non-) constant energy injection rate, etc. However, Forman et al. (2015) estimated that the expected uncertainties are only a factor of a few. Below we perform similar analysis for the central shock and bubble in the Perseus Cluster, aiming to understand whether indeed most of the AGN energy is injected into the bubbles. This energy can potentially be later transferred to the gas in the form of isobaric perturbations.

There are several features revealed by deep *Chandra* observations of the innermost region in Perseus produced by the outburst (Fig. 6a): inner bubbles with size $r \approx 7.5$ kpc, distinct shock around one of the bubbles at $r \approx 15$ kpc from the bubble centre and a shell of shock-heated gas between the bubble and the front. Modelling of the observed properties of X-ray cavities in the central ~ 25 kpc in the Perseus Cluster induced by the relativistic particles of the jet implies a time-averaged nuclear power of the order of $10^{45} \text{ erg s}^{-1}$ (e.g. Heinz et al. 1998; Churazov et al. 2000; Fabian et al. 2000). The deprojection analysis of the gas density shows a density jump

at the shock front is 1.25–1.27 (Graham et al. 2008b). Using simulations with a 1D Lagrangian code³ of a spherical shock propagating through the Perseus atmosphere, we will try to reproduce these observed features and check the energy partition that results in these simulations.

As initial, unperturbed radial profiles of the gas density and temperature in Perseus, we used the deprojected ones from Zhuravleva et al. (2013). Of course, the initial profiles that might have existed more than 10 Myr ago are quite uncertain. However, if the supermassive black hole is able to maintain a quasi-equilibrium between heating and radiative cooling and the cluster atmosphere has not undergone major changes recently, then we can hope that the present gas distribution is not far from the typical conditions at the time of the outburst. The power of the AGN is chosen so that the size of the density jump at the shock front and the ratio of the shell size to the bubble size r_{shell}/r_b approximately match the observed values. Namely, we assume a constant energy injection rate into the bubble $L_X = 3 \times 10^{44} \text{ erg s}^{-1}$ (roughly consistent with earlier estimates $\approx 5 \times 10^{44} \text{ erg s}^{-1}$ per bubble; see e.g. Heinz et al. 1998) lasting for $2 \times 10^7 \text{ yr}$. The energy injection is quenched when the bubble expansion becomes subsonic and the bubble size is $r \approx 10 \text{ kpc}$. Subsequently, the shock propagates passively through the cluster atmosphere. As an illustrative example, we show the snapshots of the density radial profiles at different time-steps and the ratio of the perturbed density to the initial one in Fig. 6(b). At $\Delta t_{\text{inject.}} = 1.1 \times 10^7 \text{ yr}$ after the injection started, the parameters of the simulated features are the closest to the observed ones (see Table 1). Accounting for uncertainties in measurements of the observed features, our conservative estimate of the lower limit on the duration of energy injection is 7 Myr. Note that 5 per cent uncertainties in the density jump and bubble size translate into ≈ 20 uncertainties in the injected power.

Our simulations provide information about the redistribution of the injected outburst energy at each time-step. When the shock is at 15 kpc from the bubble centre, the total energy released by the AGN is $\approx 10^{59} \text{ erg}$. This energy is partitioned so that it gives an excess of thermal energy within the bubble of $\approx 5 \times 10^{58} \text{ erg}$ and in the shock-heated gas of $\approx 4 \times 10^{58} \text{ erg}$ (Fig. 7). After the shock propagation, the total gravitational energy increases by $\approx 4 \times 10^{57} \text{ erg}$ and the total kinetic energy is $\approx 9.5 \times 10^{57} \text{ erg}$ in the entire $r = 15 \text{ kpc}$ region. This kinetic energy is mostly associated with the kinetic energy of the heated and compressed gas. Note that ≈ 50 per cent of the outburst energy goes into the excess thermal energy (compared to initial thermal energy) of the bubble and ≈ 38 per cent, to the excess thermal energy of the compressed and shock-heated gas. The energy in the bubble is larger than in the shell by a factor of 1.3 (the factor is 2.6 if one assumes that the gas inside the bubble is relativistic with the adiabatic index $\gamma = 4/3$). Such energy partition supports the slow-outburst scenario of the energy injection and bubble inflation.⁴ Finally, the energy carried by the shock is twice larger than the kinetic energy of the heated gas, namely $\approx 1.9 \times 10^{58} \text{ erg}$, or ≈ 18 per cent of the injected energy from the AGN (additional energy is associated with the thermal energy of the compressed gas). Note that although the energetics and parameters

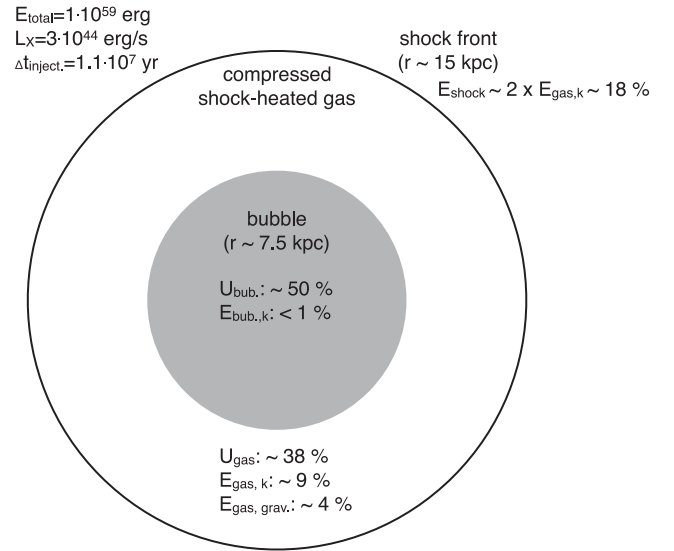


Figure 7. Sketch of the AGN-injected energy partition in the inner 15 kpc in the Perseus Cluster $\Delta t_{\text{inject.}} = 1.1 \times 10^7 \text{ yr}$ after the injection started. The results are based on 1D simulations of a spherical shock propagating through the cluster atmosphere. The energy is injected at a constant rate $L_X = 3 \times 10^{44} \text{ erg s}^{-1}$. The total energy released by the AGN up until this moment (when the shock is at 15 kpc from the bubble centre) is $E_{\text{total}} \approx 10^{59} \text{ erg}$. The input parameters are shown in the top left corner. About 50 and 38 per cent of the outflow energy is channelled to the excess thermal energies in bubble and in shock-heated gas, respectively. See Section 5.2 for details.

of the jet, shock and bubble are different from those in the Virgo Cluster (Forman et al. 2015), the way the energy from the central AGN is injected into the gas is the same in both clusters.

Our modelling implies that indeed the largest fraction of the outburst energy is stored in bubbles and a smaller fraction is transported by a shock. This result relies on the assumption that our 1D approximation and initial conditions provide a reasonable description of the cavity dynamics and the energy partition can be estimated directly from the model. A somewhat different conclusion was reached by Graham et al. (2008a), who used an extrapolation of the pressure profile from the unshocked region to smaller radii to estimate the excess energy. Their approach yields a significantly larger fraction of energy in the shock, suggesting that shock/sound waves dominate transport of energy to the ICM. Our results instead provide support to the bubble-mediated AGN feedback model (Churazov et al. 2000; McNamara et al. 2000; Forman et al. 2007; Nulsen et al. 2007; Bîrzan et al. 2012; Fabian 2012; Hlavacek-Larrondo et al. 2012). Namely, most of the energy is first stored as the enthalpy of the bubbles. As the bubbles rise buoyantly they transfer their energy to the ICM. As we show here, isobaric perturbations dominate the total variance of fluctuations, suggesting that the energy stored within the bubbles could be channelled to the ICM through gravity waves and gas motions induced during the bubble expansion and buoyant rise. The energy of the gas bulk motions eventually dissipates, providing enough heat to offset radiative cooling (Zhuravleva et al. 2014a). The data of future high-energy-resolution missions starting from ASTRO-H will be instrumental in differentiating between the two energy-transporting scenarios mentioned above.

We also looked at the properties of a sound wave produced by the central AGN propagating through the Perseus atmosphere after the energy release is quenching. Simulations show that the amplitude of a passively propagating sound wave leads to density jumps of

³ The explicit (first order in space and time) Lagrangian code was provided by H.-T. Janka. The code was initially used for supernova explosion calculations and was adopted to a cluster setup by the authors (see Forman et al. 2007).

⁴ Our experiments showed that for a given total injected energy $\sim 10^{59} \text{ erg}$, the shortening of the outburst duration leads to a stronger heating of the shock-heated gas. Time-scales shorter than 10^6 yr correspond to the limiting case of the short-outburst scenario.

Table 1. Summary of the observed features in the innermost region in the Perseus Cluster (Fig. 6) and the same parameters obtained from 1D simulations of the spherical shock propagating through the Perseus atmosphere (see Section 5.2 for details).

	Observed	Simulated
Injected jet power per bubble, L_X	$\approx 5 \times 10^{44} \text{ erg s}^{-1(1)}$	$3 \times 10^{44} \text{ erg s}^{-1}$
Position of the shock front relative to the bubble centre	$\approx 15 \text{ kpc}^{(2)}$	15 kpc
Amplitude of the density jump at the shock front	1.25–1.27 ⁽³⁾	1.25
Ratio of the shell (shock-heated gas) size to the bubble size, r_{shell}/r_b	$\approx 2^{(2)}$	1.9

(1) Boehringer et al. (1993), Heinz, Reynolds & Begelman (1998), Churazov et al. (2000), Fabian et al. (2000)

(2) Estimated from the images (see Fig. 6).

(3) Graham, Fabian & Sanders (2008b).

≈ 5 per cent at a distance of 60 kpc, which are consistent with those associated with the ripples in Perseus. At this moment, the energy is partitioned so that the contribution of the kinetic energy of these waves to the total injected energy is small, less than 8 per cent.

We emphasize that these are simple simulations and our analysis neglects many potentially important physical effects, including (but not limited to): heat conduction and viscosity (e.g. Fabian et al. 2005; Ruszkowski & Oh 2011; Gaspari et al. 2014), effects associated with shock propagation through inhomogeneous ICM (e.g. Heinz & Churazov 2005), MHD effects (e.g. Dolag, Bartelmann & Lesch 2002; Mogavero & Schekochihin 2014), the role of cosmic rays (e.g. Pfrommer et al. 2007; Brunetti & Jones 2014). Numerical and theoretical studies showed that these physical processes may strongly affect the gas properties especially on small spatial scales. For instance, strong conduction and/or large viscosity would boost the dissipation of the wave energy as it propagates through the gas, while cosmic rays could change the compressibility of the ICM, tap and redistribute the energy of the shock. However, at present it is difficult to reliably estimate the magnitude of these effects. Current results are valid in the situation when additional physical effects play a subdominant role.

6 CONCLUSIONS

In this work, we investigated the nature of AGN-driven perturbations in the core of the Perseus Cluster and determined the energetically dominant type of perturbations based on the statistical analysis of the X-ray emissivity fluctuations in soft- and hard-band images obtained from deep *Chandra* observations. We also examined how energy injected by the AGN is partitioned between different feedback channels using 1D hydro-simulations of a shock wave propagating through the Perseus Cluster atmosphere. Our main results are summarized below.

(i) The analysis of cross-spectra is able to recover the dominant type of fluctuations responsible for the fluctuations in the X-ray emissivity even if their amplitude is small, of the order of a few per cent. This is confirmed by various tests that we have carried out using both simulated and observed data.

(ii) Most of the emissivity fluctuations induced by the central AGN in the inner $\approx 140 \times 140$ kpc region have an isobaric nature (≈ 80 per cent of the total variance) on scales ~ 8 –70 kpc, i.e. are consistent with entropy variations that can result from slow displacements of the gas.

(iii) In the selected region where there are distinct ripples least contaminated by other structures, about 50 per cent of the total variance of the fluctuations is associated with isobaric perturbations on scales ~ 12 –30 kpc, supporting the stratified turbulence nature of the ripples (Zhuravleva et al. 2014a). This conclusion does not exclude the presence of ripples associated with shocks or sound

waves; however, they are energetically subdominant (≈ 5 per cent). In order to investigate the nature of individual ripples as well as to probe smaller scales using the cross-spectra analysis, at least twice longer *Chandra* observations are required. Currently, low photon statistics in the hard band limit the analysis.

(iv) Using the fact that the total variance of perturbations is proportional to the energy in perturbations, we estimated that the energy in perturbations is ~ 13 per cent of the thermal energy in the inner $r = 70$ kpc region.

(v) We also estimated the time needed to dissipate the energy from the observed fluctuations into heat to balance radiative cooling. This time is $\approx 6 \times 10^7$ – 4×10^8 yr.

(vi) Simulating the observed properties of the inner shock, bubble and shock-heated gas around the bubble in Perseus, we found that ≈ 50 per cent of the AGN-injected energy goes into the excess thermal energy of the bubble, ≈ 40 per cent goes into the compression and heating of the gas between the bubble and the shock front and ≈ 20 of the injected energy is carried away by the shock. These results are consistent with the bubble-mediated AGN feedback model and support our main results from the cross-spectrum analysis, i.e. the energetically dominant role of slow gas motions that could be induced by the bubbles through the AGN feedback.

(vii) Our simulations of the propagating shock show that the contribution of sound waves at distance of 60 kpc from the cluster centre (ripples) to the total excess energy is small, less than 8 per cent. However, a typical amplitude of the simulated ripples of a few per cent is consistent with observations.

The small number of photons, especially in the hard band, limits the analysis presented in this work. The full potential of this method will be unveiled with future X-ray observations that have large effective area (a few tens of times larger than *Chandra*), such as *Athena*⁵ and *X-ray Surveyor*.⁶ Having arcsec angular resolution with a few eV spectral resolution, both provided by *X-ray Surveyor*, will be especially helpful for probing the physics of fluctuations.

ACKNOWLEDGEMENTS

Support for this work was provided by the NASA through *Chandra* award number AR4-15013X issued by the *Chandra* X-ray Observatory Center, which is operated by the Smithsonian Astrophysical Observatory for and on behalf of the NASA under contract NAS8-03060. IZ thanks A.C. Fabian and J. Sanders for important comments and discussions. EC and AAS are grateful to the Wolfgang Pauli Institute, Vienna, for its hospitality. PA acknowledges support

⁵ <http://www.the-athena-x-ray-observatory.eu/>

⁶ http://cxc.cfa.harvard.edu/cdo/xray_surveyor/

from FONDECYT grant 1140304 and Centro de Astrofísica de Valparaíso. EC and RS are partly supported by grant No. 14-22-00271 from the Russian Scientific Foundation. We are grateful to Hans-Thomas Janka for the provision of a one-dimensional Lagrangian hydrodynamics code, initially used for supernovae explosion calculations.

REFERENCES

- Anders E., Grevesse N., 1989, *Geochimica et Cosmochimica Acta*, 53, 197
- Arévalo P., Churazov E., Zhuravleva I., Hernández-Monteagudo C., Revnivtsev M., 2012, *MNRAS*, 426, 1793
- Arévalo P., Churazov E., Zhuravleva I., Forman W. R., Jones C., 2016, *ApJ*, 818, 14
- Birzan L., Rafferty D. A., Nulsen P. E. J., McNamara B. R., Röttgering H. J. A., Wise M. W., Mittal R., 2012, *MNRAS*, 427, 3468
- Boehringer H., Voges W., Fabian A. C., Edge A. C., Neumann D. M., 1993, *MNRAS*, 264, L25
- Brunetti G., Jones T. W., 2014, *Int. J. Modern Phys. D*, 23, 1430007
- Churazov E., Forman W., Jones C., Böhringer H., 2000, *A&A*, 356, 788
- Churazov E., Brüggemann M., Kaiser C. R., Böhringer H., Forman W., 2001, *ApJ*, 554, 261
- Churazov E., Sunyaev R., Forman W., Böhringer H., 2002, *MNRAS*, 332, 729
- Churazov E. et al., 2012, *MNRAS*, 421, 1123
- Dennis T. J., Chandran B. D. G., 2005, *ApJ*, 622, 205
- Dickey J. M., Lockman F. J., 1990, *ARA&A*, 28, 215
- Dolag K., Bartelmann M., Lesch H., 2002, *A&A*, 387, 383
- Fabian A. C., 2012, *ARA&A*, 50, 455
- Fabian A. C. et al., 2000, *MNRAS*, 318, L65
- Fabian A. C., Sanders J. S., Allen S. W., Crawford C. S., Iwasawa K., Johnstone R. M., Schmidt R. W., Taylor G. B., 2003, *MNRAS*, 344, L43
- Fabian A. C., Reynolds C. S., Taylor G. B., Dunn R. J. H., 2005, *MNRAS*, 363, 891
- Fabian A. C., Sanders J. S., Taylor G. B., Allen S. W., Crawford C. S., Johnstone R. M., Iwasawa K., 2006, *MNRAS*, 366, 417
- Fabian A. C. et al., 2011, *MNRAS*, 418, 2154
- Forman W. et al., 2007, *ApJ*, 665, 1057
- Forman W. et al., 2015, in press
- Gaspari M., Churazov E., Nagai D., Lau E. T., Zhuravleva I., 2014, *A&A*, 569, A67
- Graham J., Fabian A. C., Sanders J. S., 2008a, *MNRAS*, 391, 1749
- Graham J., Fabian A. C., Sanders J. S., 2008b, *MNRAS*, 386, 278
- Gu L. et al., 2009, *ApJ*, 700, 1161
- Heinz S., Churazov E., 2005, *ApJ*, 634, L141
- Heinz S., Reynolds C. S., Begelman M. C., 1998, *ApJ*, 501, 126
- Hillel S., Soker N., 2014, *MNRAS*, 445, 4161
- Hlavacek-Larrondo J., Fabian A. C., Edge A. C., Ebeling H., Sanders J. S., Hogan M. T., Taylor G. B., 2012, *MNRAS*, 421, 1360
- Kalberla P. M. W., Burton W. B., Hartmann D., Arnal E. M., Bajaja E., Morras R., Pöppel W. G. L., 2005, *A&A*, 440, 775
- Kawahara H., Suto Y., Kitayama T., Sasaki S., Shimizu M., Rasia E., Dolag K., 2007, *ApJ*, 659, 257
- Kim W.-T., Narayan R., 2003, *ApJ*, 596, L139
- Landau L. D., Lifshitz E. M., 1959, *Course of Theoretical Physics*. Pergamon Press, Oxford
- McNamara B. R., Nulsen P. E. J., 2007, *ARA&A*, 45, 117
- McNamara B. R. et al., 2000, *ApJ*, 534, L135
- Mogavero F., Schekochihin A. A., 2014, *MNRAS*, 440, 3226
- Nulsen P., McNamara B. R., David L. P., Wise M. W., Leahy J. P., 2007, *A&AS*, 39, 148
- Omma H., Binney J., Bryan G., Slyz A., 2004, *MNRAS*, 348, 1105
- Ossenkopf V., Krips M., Stutzki J., 2008, *A&A*, 485, 917
- Pfrommer C., 2013, *ApJ*, 779, 10
- Pfrommer C., Enßlin T. A., Springel V., Jubelgas M., Dolag K., 2007, *MNRAS*, 378, 385
- Randall S. W. et al., 2015, *ApJ*, 805, 112
- Reynolds C. S., Balbus S. A., Schekochihin A. A., 2015, *ApJ*, 815, 41
- Ruszkowski M., Oh S. P., 2011, *MNRAS*, 414, 1493
- Ruszkowski M., Enßlin T. A., Brüggemann M., Heinz S., Pfrommer C., 2007, *MNRAS*, 378, 662
- Sanders J. S., Fabian A. C., 2007, *MNRAS*, 381, 1381
- Sanders J. S., Fabian A. C., 2012, *MNRAS*, 421, 726
- Schuecker P., Finoguenov A., Miniati F., Böhringer H., Briel U. G., 2004, *A&A*, 426, 387
- Sharma P., Chandran B. D. G., Quataert E., Parrish I. J., 2009, *ApJ*, 699, 348
- Soker N., Hillel S., Sternberg A., 2015, preprint ([arXiv:1504.07754](https://arxiv.org/abs/1504.07754))
- Walker S. A., Sanders J. S., Fabian A. C., 2015, *MNRAS*, 453, 3699
- Werner N., Urban O., Simionescu A., Allen S. W., 2013, *Nature*, 502, 656
- Zhuravleva I. et al., 2013, *MNRAS*, 435, 3111
- Zhuravleva I., Churazov E., Kravtsov A., Lau E. T., Nagai D., Sunyaev R., 2013, *MNRAS*, 428, 3274
- Zhuravleva I. et al., 2014a, *ApJ*, 788, L13
- Zhuravleva I. et al., 2014b, *Nature*, 515, 85
- Zhuravleva I. et al., 2015, *MNRAS*, 450, 4184

APPENDIX A: CHOICE OF ENERGY BANDS

Depending on the choice of bands, the flux ratios [Fig. 1, equation (6)] in pure adiabatic and isobaric cases shift closer to or further away from each other. The harder the hard band and/or the larger the gap between the soft and hard bands, the larger the difference between the adiabatic and isobaric ratios. Therefore, the energy bands of the X-ray images used in the analysis are chosen based on two simple criteria: (i) the larger the difference between the adiabatic and isobaric curves in Fig. 1 the more powerful the diagnostic of fluctuations of different types, i.e. the difference

$$\Delta w = \frac{w_{b, \text{adiab.}}}{w_{a, \text{adiab.}}} - \frac{w_{b, \text{isob.}}}{w_{a, \text{isob.}}} \quad (\text{A1})$$

is large; (ii) bands should be broad enough so that the uncertainties in the cross-spectrum due to noise are small. In the limit of noise-dominated data the ability to detect the difference between adiabatic and isobaric fluctuations depends on the ratio $\Delta w / \sigma_a \sigma_b$, where $\sigma_{a(b)} \propto 1 / \Lambda_{a(b)}^{1/2}$ are the Poisson errors in the images, divided by the smooth model. Therefore, those bands that give the maximal value of the ratio

$$\frac{\Delta w}{\sigma_a \sigma_b} = \left[\frac{w_{b, \text{adiab.}}}{w_{a, \text{adiab.}}} - \frac{w_{b, \text{isob.}}}{w_{a, \text{isob.}}} \right] (\Lambda_a \Lambda_b)^{1/2} \quad (\text{A2})$$

should be chosen. Both criteria showed that the 0.5–4 keV and 4–8 keV combination is the optimal choice. Experiments with other, similarly good bands, gave results consistent with those presented in the main text.

APPENDIX B: C AND R IN THE CASE OF LARGE-AMPLITUDE FLUCTUATIONS

Maps of coherence C and ratio R (Figs 3 and 5) are calculated under the assumption of small amplitude fluctuations. In order to check how robust these predictions for larger amplitudes are, we carried out simple simulations. Assuming that density fluctuations along the line of sight have a lognormal distribution as suggested by numerical simulations (Kawahara et al. 2007; Zhuravleva et al. 2013), we generated density fluctuation patterns as

$$\frac{n + \delta n}{n} = e^{A\xi}, \quad (\text{B1})$$

where A is a parameter characterizing the amplitude of fluctuations and ξ is a random, normally distributed variable with a zero

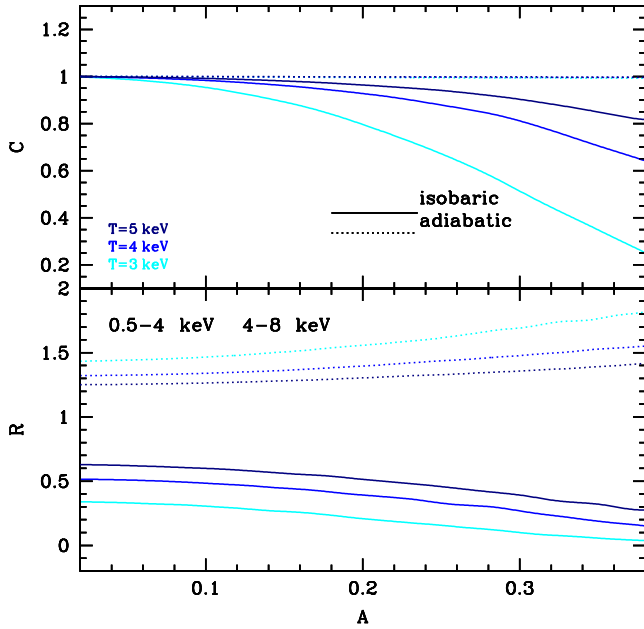


Figure B1. Coherence C and ratio R of emissivity fluctuations in two energy bands, 0.5–4 keV and 4–8 keV, as a function of a parameter A , which characterizes the amplitude of lognormal density fluctuations modelled by equation (B1), for three different gas temperatures in the cases of pure isobaric or adiabatic fluctuations. Note that in the adiabatic case, C does not vary much with the amplitude of fluctuations (as expected) or with gas temperature, in contrast to the isobaric case. For $A \lesssim 0.15$ both C and R only weakly depend on A if the gas is hotter than 3 keV.

mean and standard deviation 1. Corresponding temperature fluctuations are $(T + \delta T)/T = [(n + \delta n)/n]^{\zeta_i - 1}$, where $\zeta_i = 5/3$, 0 and 1 for adiabatic, isobaric and isothermal fluctuations, respectively. Assuming that there are many fluctuations along the line of sight, we obtain emissivity perturbations $\delta f/f$ in the soft and hard bands and measure C and R shown in Fig. B1. Both C and R are consistent with the values in the limit of small-amplitude perturbations [equation (6), Figs 1, 3 and 5] as long as the value of A in the gas with $T > 3$ keV is $\lesssim 15$ per cent. Also, C in the cases of pure isobaric and adiabatic fluctuations is almost the same, while R is different in all three cases. Therefore, R is a better diagnostic for differentiation between different types of perturbation in the gas with Perseus-like temperatures than C .

APPENDIX C: CROSS-SPECTRA ANALYSIS OF SIMULATED IMAGES WITH SHOCK AND SOUND WAVES

An interesting question is whether the cross-spectra method is able to determine correctly the dominant type of perturbations if their amplitude is small, viz., a few per cent. Using simulated density and temperature radial profiles shown in Fig. 6(b), we obtained the X-ray images in soft and hard bands when the shock was at 15 and 60 kpc (see Section 5.2). Fig. C1 shows the radial profiles of the X-ray surface brightness in both cases. Note a clear discontinuity in the surface brightness when the shock is at 15 kpc and a barely noticeable kink when the shock is at 60 kpc.

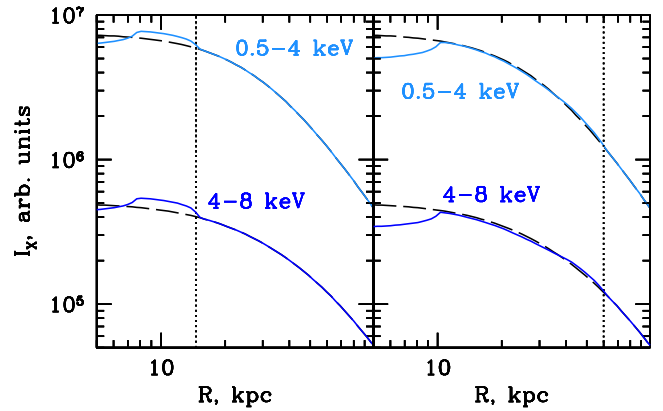


Figure C1. Simulated radial profiles of the X-ray surface brightness I_X in the 0.5–4 keV and 4–8 keV bands, calculated from the density and temperature radial profiles modified by the propagating spherical shock in the Perseus Cluster (see Fig. 6b). The unperturbed profiles are shown with black dashed curves. Left: shock at 15 kpc from the bubble centre. Right: shock at 60 kpc.

We fit the profiles with β -models, obtained the residual images of the surface brightness fluctuations and repeated the cross-spectra analysis by measuring the amplitude of the volume emissivity fluctuations in both bands, the cross-amplitude, the correlation C and the ratio R . The results are shown in Fig. C2.

First, we analysed fluctuations in the annulus with a width of 0.8 arcmin around the shock at 15 kpc. The annulus width roughly matches the size of the region with the shock in the observed images that we considered earlier (see Fig. 2). The amplitude of emissivity fluctuations is ≈ 26 per cent and ≈ 14 per cent (Fig. C2) at ~ 10 kpc scales in the soft and hard bands, respectively. These values are close to those obtained from observations in the extraction region of similar size. If wider annulus is used, the amplitudes derived from simulations go down compared to observations because in the latter, other perturbations besides the shock front contribute to the surface-brightness fluctuations. In contrast, the measured coherence and ratio are very stable. The measured coherence $C \approx 1$ (Fig. C2) confirms the presence of only one type of perturbations. The ratio $R \sim 1.9$ at 10 kpc scale is slightly higher than the predicted value 1.4–1.6 (Fig. 1). This deviation can be due to the temperature variations in the chosen region and the relatively large amplitude of emissivity fluctuations. Also the choice of the underlying model may affect the results, especially on large scales. Nevertheless, we can confidently exclude perturbations of an isothermal ($R = 1$) or isobaric ($R < 0.4$) nature.

For the sound wave at 60 kpc, we consider a broader annulus of width 1.6 arcmin, which roughly matches the size of the dotted region in Fig. 4. The measured amplitudes of the emissivity fluctuations are ~ 4.5 and ~ 6 per cent on scales of ~ 20 kpc in the soft and hard bands, respectively (Fig. C2), which are lower than the observed value, ~ 12 per cent, in Perseus (Fig. 5). The measured amplitude strongly depends on the size of the region analysed. However, both $C \approx 1$ and $R \approx 1.2$ robustly confirm the adiabatic nature of the perturbations. This test shows that the cross-spectra analysis is powerful enough to determine the dominant type of perturbations even if the amplitude of emissivity fluctuations is only a few Per cent.

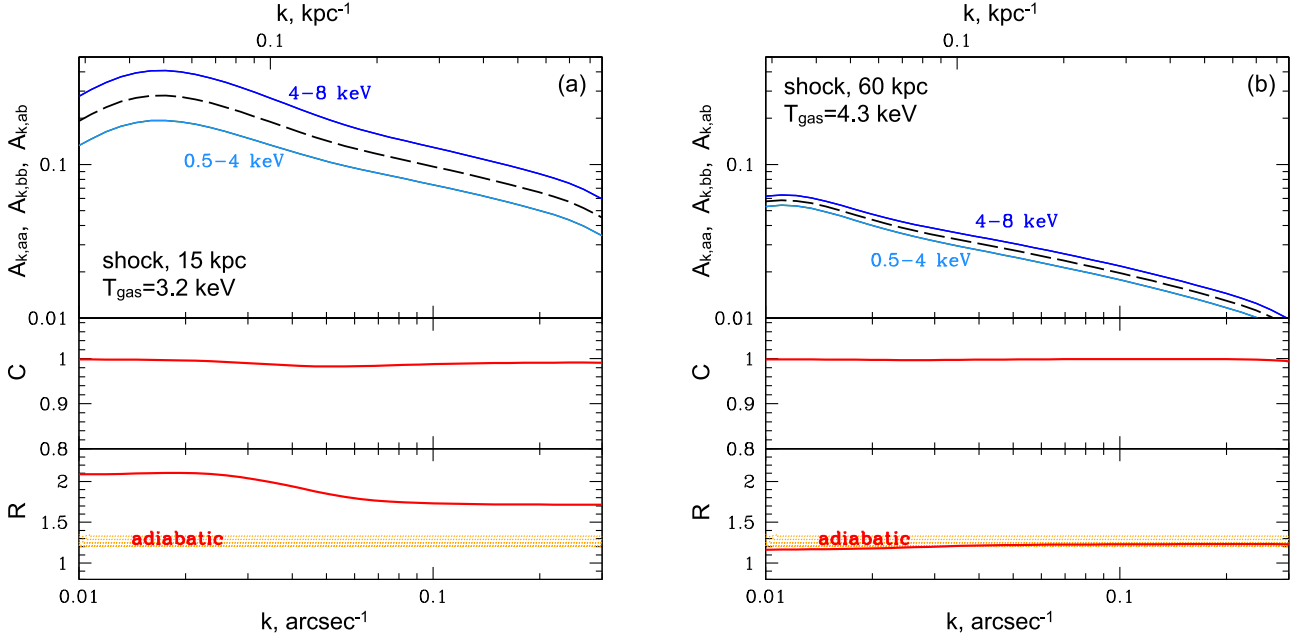


Figure C2. Cross-spectra analysis of simulated images with a shock/sound wave (see Figs 6 b and C1). The amplitude of emissivity fluctuations in both bands and the cross-amplitude are shown in the top panels. Correlation coefficient C and ratio R are shown in the middle and bottom panels, respectively. Expected R (Fig. 1) for pure adiabatic fluctuations is shown with orange regions. (a) Shock at 15 kpc. The analysis is done in the annulus around the shock with the width 0.8 arcmin. (b) Sound wave at 60 kpc. The width of the annulus used for the analysis is 1.6 arcmin. The cross-spectra analysis captures the adiabatic nature of the perturbation in both cases, even if the amplitude of the emissivity fluctuations is small (a few per cent).

This paper has been typeset from a \LaTeX file prepared by the author.